Analysis of the ALMA Telescope and Front-ends

S.B. Sørensen*, K. Pontoppidan
TICRA, Copenhagen, Denmark
*Contact: ticra@ticra.com, phone +45-33-12-4572

***Abstract*— The purpose of the present study is to provide a more detailed electromagnetic analysis of the telescope optics than previously performed, including support leg blockage effects, detailed reflector geometry, surface deformations and front-end analyses. Radiation patterns including these effects are calculated for all frequency bands.**

I. Introduction

The ALMA (Atacama Large Millimeter Array) project is an array of 12-meter radio astronomy telescopes now being assembled in the high-altitude Atacama desert in Chile. A very large bandwidth is covered by the array since each telescope includes 10 receiver front-ends that operate from 30 to 950 GHz. TICRA became involved in ALMA through a contract with ESO. Our work started late in the ALMA project after the design of the telescope and most of the front-ends was established, so our role was to provide accurate verification of the optical design and to calculate the detailed performance of the total telescope system for all frequency bands. The paper will present a summary of the analysis of both the front-ends and the telescope with emphasis on the most challenging and critical aspects of the optics system. Further details can be found in [1] and [2]. All analyses have been carried out by the TICRA software tools GRASP [3] and CHAMP for reflector antennas and corrugated horns, respectively. These tools use accurate and well established numerical methods, such as Physical Optics, the Method of Moments and Mode Matching.

II. Front-end Analysis

The total frequency bandwidth of the ALMA telescopes is extremely wide (from 30 to 950 GHz) which necessitates a complicated front-end with 10 separate receiver systems for different frequency sub-bands. The sub-bands are numbered from 1 to 10. As a typical example, the band 6 front-end is illustrated in Fig. 1 and operates in the range from 211 to 275 GHz. The optics is located in a cryostat and consists of a corrugated horn and two ellipsoidal mirrors. The apertures corresponding to two thermal filters and a cryostat window are also shown in the figure.

The design of such front-end optics is conveniently carried out by Gaussian beam techniques by which a number of beam parameters can be computed and optimized. More accurate methods are, however, needed for verification of the design.

The corrugated horn designs have for some bands been verified by the CHAMP mode-matching software by which the performance over the full frequency band can be calculated with high accuracy, including cross polarization and return loss.

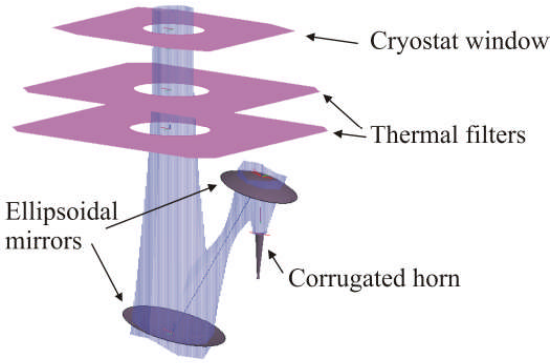

Fig. 1 Band 6 front-end optics.

A detailed analysis of the ellipsoidal mirrors was carried out for all bands by means of Physical Optics using the GRASP software. This gives an accurate prediction of the beam shape, cross-polarization, beam truncation and diffraction at the edges of the mirrors and spill-over loss. The filter and cryostat windows were treated as apertures in screens to determine possible beam truncation effects, whereas reflection and loss in the filter and window material was found from measured data.

A. Feed Lens Analysis

The band 3 front-end operates from 84 to 116 GHz and is shown in Fig. 2. Due to the relatively low frequency the mirrors become large and must be located above the filters and cryostat window and thus outside the cryostat. The limited space also necessitates a short corrugated horn supplemented with a phase correcting plano-convex dielectric lens. A close-up of the horn+lens is shown in Fig. 3.

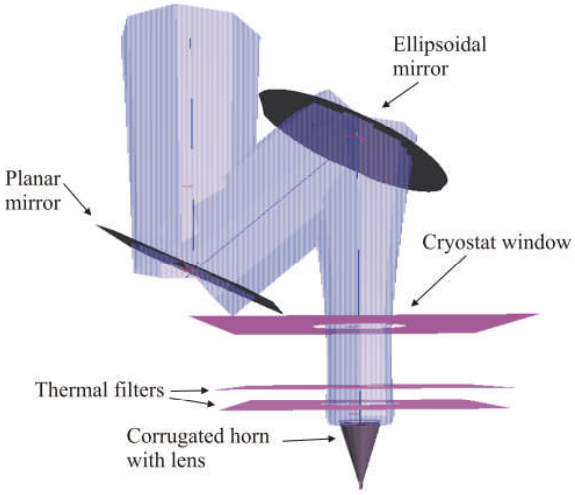

Fig. 2 Band 3 front-end optics.

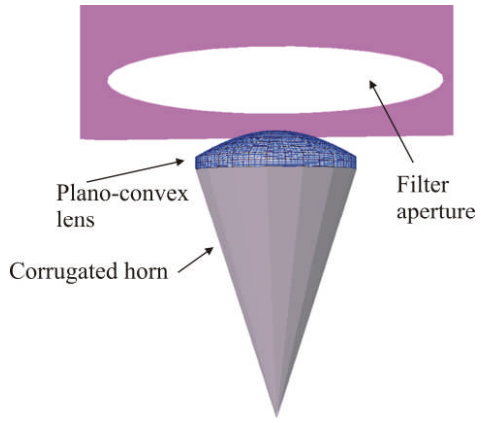

Fig. 3 Band 3 horn with lens.

The analysis procedure was mode-matching for the corrugated horn, a plane-wave expansion to transform the far field of the horn to the lower surface of the lens and then the Method of Moments for analysis of the lens. A special complication is the concentric grooves in the lens as shown in Fig. 4 which act as matching layers. Such grooves cannot be modelled with Physical Optics, but can be handled very accurately by the Method of Moments.

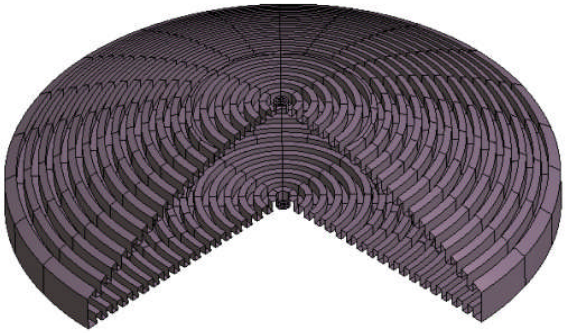

Fig. 4 Band 3 lens with grooves.

The effect of the grooves on the co-polar pattern is shown in Fig. 5 and the cross-polar pattern is shown in Fig. 6. It is seen that the grooves give a very significant reduction of the reflection from the lens, but that the cross-polar maximum is increased by app. 10 dB. It is also seen that such detailed modelling is very important for accurate prediction of the performance.

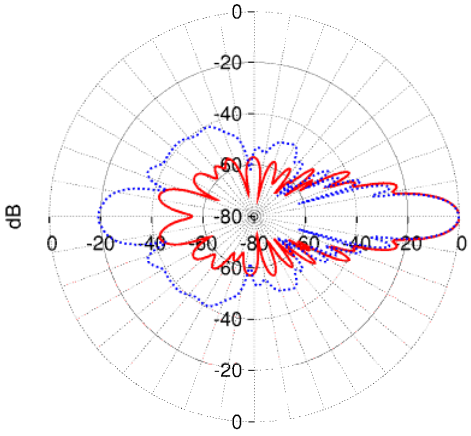

Fig. 5 Band 3 Feed+lens co-polar pattern
Blue curve: Smooth lens
Red curve: Lens with grooves

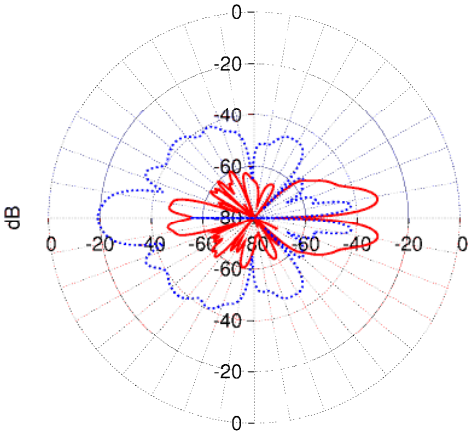

Fig. 6 Band 3 Feed+lens cx-polar pattern
Blue curve: Smooth lens
Red curve: Lens with grooves

B. Polarization Grids

In some of the front-ends, e.g. band 7, a polarization grid is used to split the incoming beam in two polarizations which are directed to two different corrugated horns. The geometry of band 7 is shown in Fig. 7.

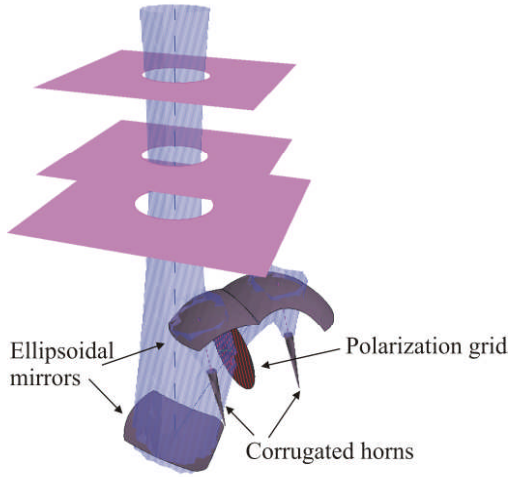

Fig. 7 Band 7 Front-end optics.

The polarization grid is constructed as thin strips located on a dielectric support layer. The maximum spacing of these strips must be app. λ/20 for good performance. In GRASP the analysis of such structures is carried out by means of plane-wave reflection and transmission coefficients. For simple layers (dielectrics, strip grids [4], etc.) the reflection and transmission coefficients are known and the total coefficients for a layered sandwich structure can be found by a cascade coupling of the reflection and transmission matrices (i.e. S-matrices [3]). Since the incident field on the grid is not a single perfect plane wave an accurate analysis requires expansion of the incident field in a spectrum of plane waves of the form

$$\boldsymbol{E}(\boldsymbol{r}) = \sum_i \boldsymbol{q}_i e^{-j\boldsymbol{k}_i \cdot \boldsymbol{r}} \qquad (1)$$

where $\boldsymbol{E}$ is the incident field, $\boldsymbol{r}$ is the observation point, and $\boldsymbol{q}_i$ and $\boldsymbol{k}_i$ are the plane-wave amplitude and propagation vectors, respectively. The analysis proceeds by treating each plane wave separately such that reflection and transmission coefficients are computed for each plane wave. The resulting reflected and transmitted fields are then converted to equivalent electric and magnetic currents which can finally be added and integrated. This procedure is necessary for an accurate treatment of the grid and also reveals significant difference in performance of the two grid orientations shown in Fig. 8 and Fig. 9. The grid in Fig. 8, where the strips are orthogonal to the centre beam direction performs better than the other possibility in Fig. 9, where the grid lines are parallel to the plane define by the incident and reflected centre rays.

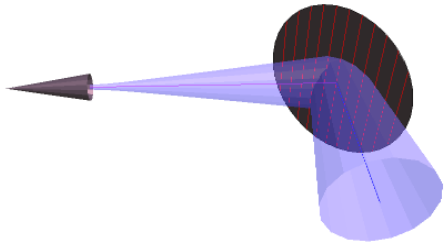

Fig. 8 Strip grid with orientation orthogonal to the plane of incidence.

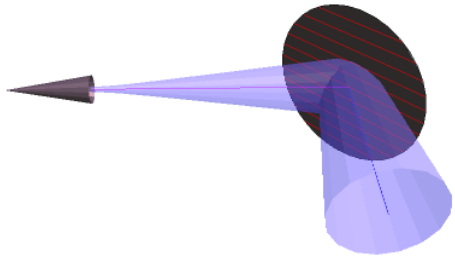

Fig. 9 Strip grid with orientation parallel to the plane of incidence.

C. *Front-end Efficiencies*

The final step in the front-end analysis was an efficiency calculation that turned out to be of great interest for ESO. Here the front-end performance is subdivided into a number of efficiencies, i.e. amplitude, phase, spill-over and polarization efficiency. In this way it becomes easier to overview the performance and point to possible weaknesses in the front-end. In some cases this has suggested minor modifications and fine-tuning of the optical systems.

The peak directivity of the telescope can be written as

$$\frac{4\pi A}{\lambda^2}\eta_{spill-over}\eta_{polarization}\eta_{amplitude}\eta_{phase} \qquad (2)$$

where the first factor $4\pi A/\lambda^2$ is the ideal maximum directivity for an aperture of area A. The remaining four factors are efficiencies for spill-over, polarization, amplitude and phase, respectively. They can be calculated from

$$\begin{aligned} \eta_{spill-over} &= I_1 / (4\pi) \\ \eta_{polarization} &= I_2 / I_1 \\ \eta_{amplitude} &= I_3^2 / (\Omega I_2) \\ \eta_{phase} &= I_4^2 / I_3^2, \end{aligned} \qquad (3)$$

where Ω is the solid angle subtended by the subreflector and the I's are the integrals

$$I_1 = \int_\Omega |\, \boldsymbol{E}_{tot} \,|^2 \, d\omega$$

$$I_2 = \int_\Omega |\, \boldsymbol{E}_{co} \,|^2 \, d\omega$$

$$I_3 = \int_{\Omega} | \boldsymbol{E}_{co} | \, d\omega \qquad (4)$$

$$I_4 = | \int_{\Omega} \boldsymbol{E}_{co} d\omega \, |$$

Here the integrals are calculated over the solid angle Ω, with $d\omega$ as the solid angle element and $\boldsymbol{E}_{tot}$ and $\boldsymbol{E}_{co}$ as the total and co-polar E-field, respectively, from the front-end.

As an example the efficiencies for band 7 are shown in Table I.

TABLE I
BAND 7 EFFICIENCIES

Band 7	$\eta_{\text{spill-over}}$	η_{pol}	η_{amp}	η_{phase}	η_{total}
324 GHz x-pol y-pol	 0.9370 0.9377	 0.9932 0.9932	 0.9018 0.9033	 0.9996 0.9995	 0.8389 0.8409
Gauss Beam	0.9399	1.0000	0.8624	1.0000	0.8106

It is seen that the front-end is well designed with high polarization and phase efficiencies, and a good compromise between spill-over and amplitude efficiency. It is also seen that the numbers obtained with the ideal Gaussian beam feed pattern (as used in the synthesis) deviates significantly from the realistic values. Although the Gaussian beam analysis is very useful in the design phase a detailed Physical Optics analysis is thus necessary for verification of the design.

III. TELESCOPE ANALYSIS

One of the telescopes is shown in Fig. 10. The main reflector is 12 m in diameter with a centre hole of 0.75 m and it consists of 120 or 264 panels, depending on the manufacturer. The subreflector is 0.75 m in diameter and it is supported by four struts. The front-ends are located 1.3 m behind the main reflector apex. The subreflector is supplied with a central tip corresponding to the hole in the main reflector.

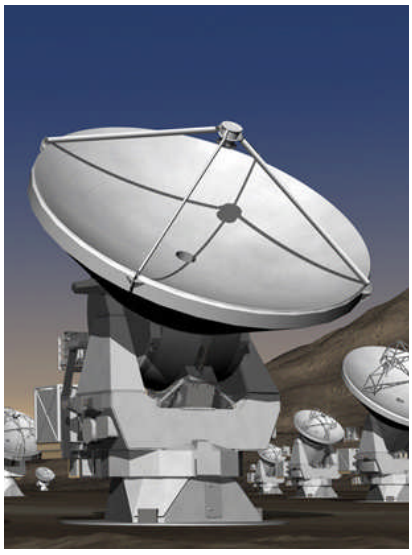

Fig. 10 ALMA telescope

Besides the nominal telescope performance TICRA also calculated a number of individual effects such as strut scattering (from the four support legs, see Fig. 10) and surface tolerance effects. This will be described in the following subsections.

A. Strut Effects

In Fig. 11 the scattering from a single strut is illustrated. An incident field from the telescope mirror (a nearly plane wave) will induce a set of currents on it, which in turn radiates a field illustrated by the red rays in Fig. 11. At each point on the struts the rays form a scattering cone with a half apex angle of $v = 62°$. In the vertical direction these rays will be in opposite phase of the main beam and give a small reduction of the peak directivity. Most of the rays will hit the cold sky either directly or through reflection in the mirror as show in Fig. 11, but in a small angular region it is, however, possible that the rays hit the ground which generates noise.

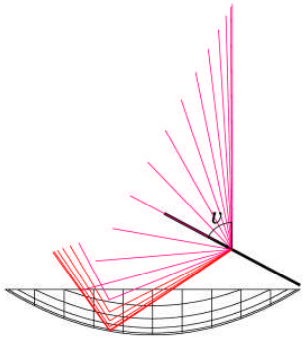

Fig. 11 Strut cross-section

The strut cross-section is elliptical and it is supplied with a cladding to improve the noise performance as shown in Fig. 12. This cladding is undesirable from a mechanical point of view and one task for TICRA was to determine how much it improves the noise performance in order to find out if the added mechanical complexity is justified.

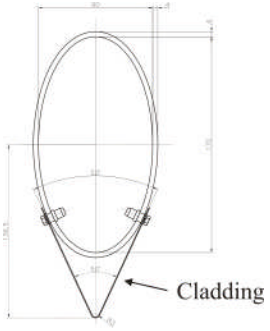

Fig. 12 Strut cross-section

The field from the scattered rays in Fig. 11 is shown in Fig. 13, with and without cladding. Both versions give the same shadowing effect near the boresight direction but away from this direction the elliptical strut gives an almost constant field of 15 dBi. However, the cladding gives rise to

two significant effects. The planar facets of the cladding generates high peaks at 50° on the diffraction cone and above this angle the field is about 10 dB lower than without cladding.

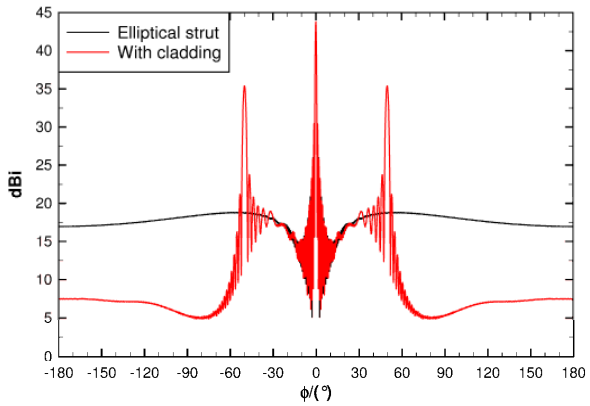

Fig. 13 Strut scattering and effect of the cladding

The angle ϕ in Fig. 13 is measured around the strut with ϕ=0° as the boresight direction. With θ=0° as the axis of the strut in a standard polar coordinate system it turns out that a significant noise contribution from the ground is only obtained in the interval from 106.4° to 147.5° in ϕ and from 61.9° to 62.1° in θ. For all struts this gives a noise contribution of 0.15°K with cladding and 1.72°K without cladding. From these results it was decided that the cladding was necessary.

B. *Influence of Reflector Panels*

This section describes the influence of the fact that the main reflector consists of a number of panels separated by a certain gap. The goal is to quantify the influence of the gaps. It is assumed that the surface of each panel is identical to that of the parent paraboloid and the feed is located at the focus of the antenna system.

A typical layout of the panels for the main reflector is shown in Fig. 14. The reflector consists of 120 panels located in 5 rings. The width of all gaps, both radial and circumferential, is 1.5 mm.

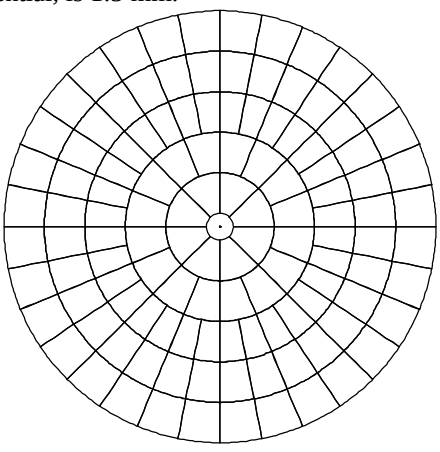

Fig. 14 Typical layout of the main reflector panels.

Fig. 15 shows the radiation patterns for the solid main reflector in black and for the reflector with panels in red. It is seen that the two patterns are almost identical and the difference pattern in green shows that the influence of the panels is around 70 dB below peak everywhere, except in the beam direction where the panel influence is determined by the gap area, approximately 50 dB below peak. The panel gaps reduce the peak gain by only 0.03 dB.

This result shows that the influence from the panel gaps is very small. This is an important conclusion because it means that all calculations can be carried out for a solid main reflector. The only exception is where the panel mounting errors are investigated and where it is obviously necessary to perform the calculations on the individual panels.

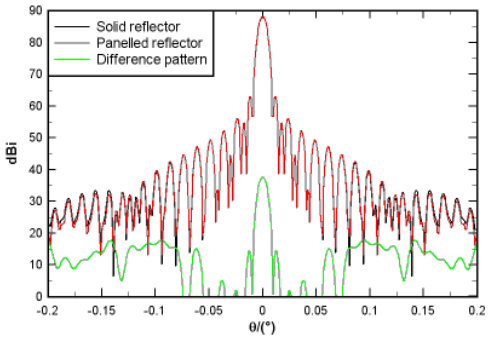

Fig. 15 The influence of the panels for the main reflector. 230 GHz.

C. *Main Reflector Surface Errors*

1) *Gravitation Effects*

The main reflector surface will deform due to gravitation, wind and thermal gradients. Here the deformations due to gravitation for 0° elevation are considered. Fig. 16 shows the deformed surface relative to the nominal paraboloid. The unit on the z-axis is mm. It is seen that there is a significant difference, in the order of 0.5 mm at the edge. From the deformed surface it is possible to find a best fit paraboloid. It has six degrees of freedom: the vertex position in x, y and z, the focal length and the axis direction.

Fig. 17 shows the best fit paraboloid relative to the nominal paraboloid and it is seen that most of the deviations in Fig. 16 are very well represented by the best fit paraboloid.

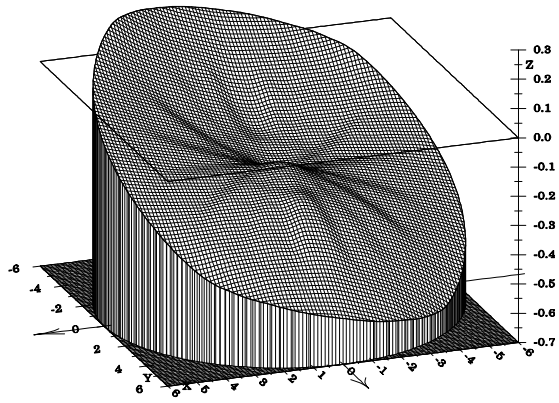

Fig. 16 The deviation between the nominal paraboloid and the reflector subject to gravitation, 0° elevation.

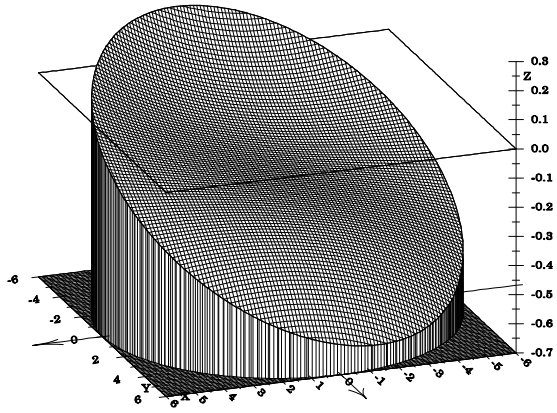

Fig. 17 The deviation between the nominal and the best fit paraboloid, 0º elevation.

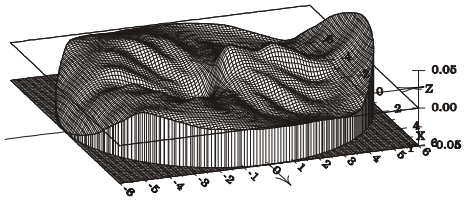

Fig. 18 The deviation between the deformed reflector and the best fit paraboloid, 0º elevation.

In other words, the reflector deformations change the nominal paraboloid into another paraboloid. Fig. 18 shows the remaining surface errors as the difference between the real deformed surface and the best fit paraboloid. The maximum deviation is here only about 50 μm and the rms error has been calculated to 12 μm.

The following plots illustrate the influence from the gravitation effects on the radiated beam. Fig. 19 and 20 show, as an example, the contour plots both for the nominal antenna and for gravitation deformation at 0º elevation at 243 GHz. The four support struts for the subreflector are also included in these calculations and this is the reason for the four-fold symmetry in the contour plots.

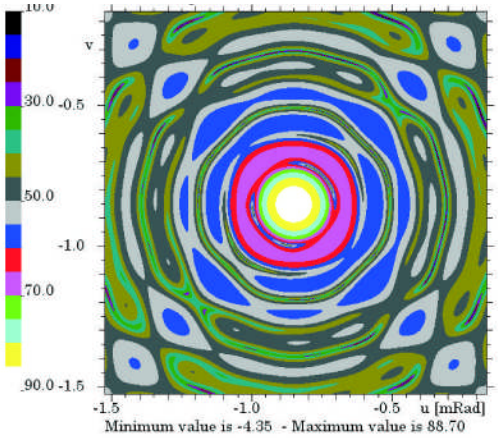

Fig. 19 Contour plot of the nominal beam at 243 GHz. Struts included.

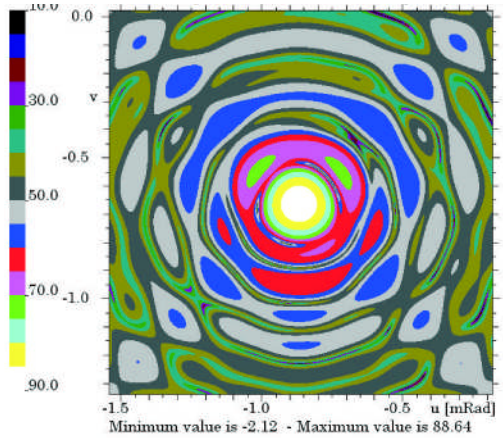

Fig. 20 Contour plot of the gravitation deformed beam at 243 GHz. Struts included.

The same type of plots is shown in Fig. 21 and 22 for 720 GHz. It is clearly seen that the surface deformations are much more critical at the highest frequency. The gain reduction is only 0.06 dB at 243 GHz whereas it increases to 0.50 dB at 720 GHz.

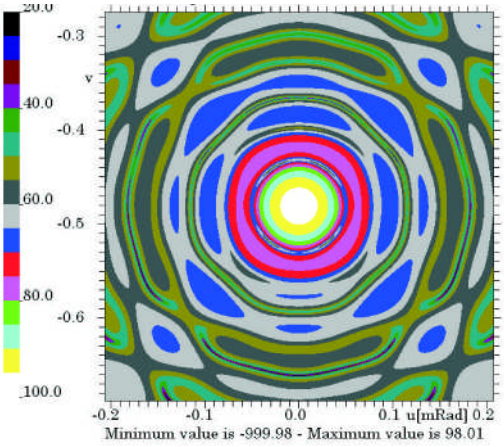

Fig. 21 Contour plot of the nominal beam at 720 GHz. Struts included.

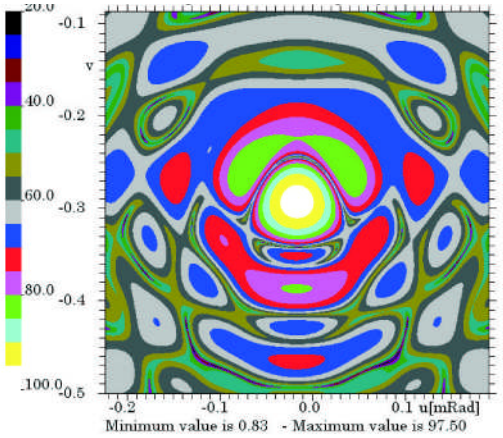

Fig. 22 Contour plot of the gravitation deformed beam at 720 GHz. Struts included.

2) Panel Surface and Alignment Errors

As mentioned earlier, the influence of the panel gaps is very small when the surface shape and alignment of the panels is ideal. In this section both panel deformation and panel alignment errors will be presented.

Based on information from the antenna supplier it was decided to model the panel shape error as a smooth random distortion all over the reflector with an rms error of 8 μm and a correlation distance approximately equal to the panel size.

Each panel is attached at five attachment points and the accuracy at these points is assumed to be 5 μ m. A random number generator is used to model the errors at the attachment points. The alignment errors are modelled by tilting each panel individually, without changing its shape, such that it passes through the five points in the best possible way. The principle is illustrated in Fig. 23 where the errors are increased by a factor 10000.

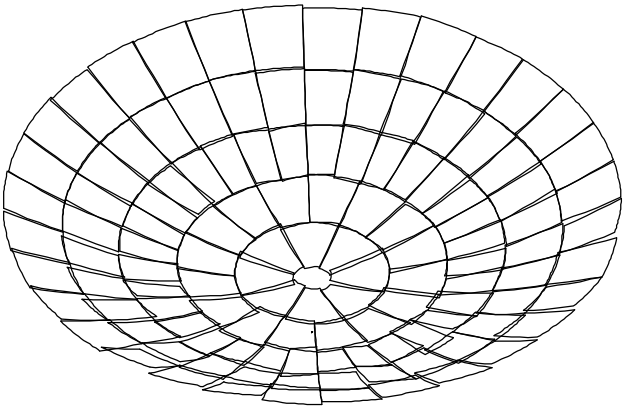

Fig. 23 Main reflector illustrating the panel alignment errors. The realistic errors are multiplied by 10,000 in this figure.

Figures 24 and 25 show contour plots and pattern cuts for the two types of panel errors separately: the manufacturing errors affecting the shape of the panels and the alignment errors affecting the orientation of the panels. Since the impact of these errors is quite small only the results for 720 GHz are presented. The reduction in gain at 720 GHz is 0.18 dB and 0.03 dB for manufacturing and alignment errors, respectively. The corresponding numbers at 243 GHz are 0.02 and 0.00 dB.

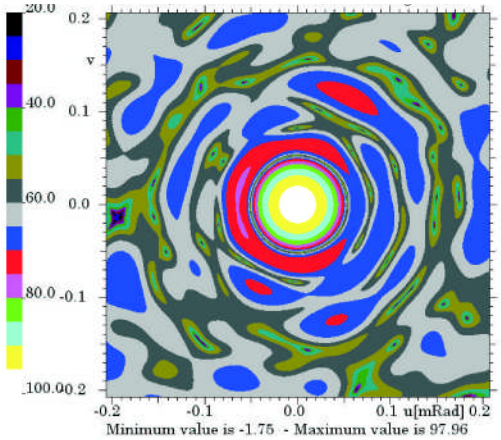

Fig. 24 Contour plot of the beam at 720 GHz for the antenna with panel manufacturing errors.

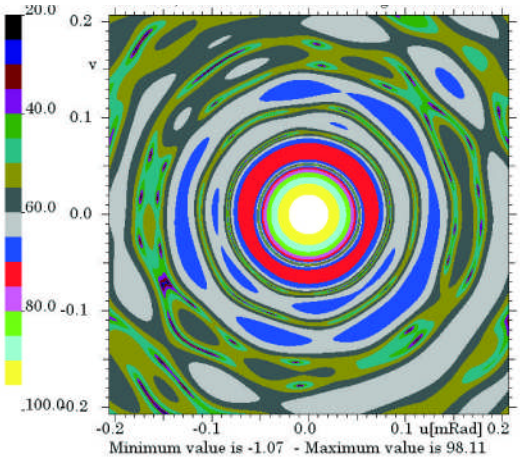

Fig. 25 Contour plot of the beam at 720 GHz for the antenna with panel alignment errors.

IV. Conclusions

In the present study it is demonstrated that it is possible to do a detailed electromagnetic analysis of the ALMA telescope optics with standard software tools. Detailed performance of the front-ends as well as the telescope mirrors can be computed by means of accurate diffraction methods, such as Physical Optics and the Method of Moments. It is also possible to take into account various distortion effects from e.g. struts and mirror surface errors.

References

[1] K. Pontoppidan, *Electromagnetic properties and optical analysis of the ALMA antennas and Front Ends*, TICRA report No. S-1430-02, ALMA doc. Number: ALMA-80.04.00.00-026-A-REP January 2008.

[2] M. Carter, *ALMA Front-end Optics Design Report*, FEND-40.02.00.00-035-B-REP, June, 2007.

[3] K. Pontoppidan, *GRASP Technical Description, Downloadable from* www.ticra.com

[4] K. Nakamura and M. Ando, *A Full–wave Analysis of Offset Reflector Antennas with Polarization Grids"*, IEEE trans. Antennas Propagat., Vol. 36, No. 2, pp. 164-170, 1988.